Supporting Information

Unidirectional ion transport induced moisture-electric generation with persistent current output for self-powered monitoring system

Shunli Wu†[a], Bingsen Wang†[b], Xiaohu Ren[a]*, Hongfeng Yin[a], Hudie Yuan[a], Mingchang Zhang[c]*, Yuchi Liu[a], Zhijun Wu[c], Wengang Cui[c], Lin Li[b]*

a. College of Materials Science and Engineering, Xi'an University of Architecture and Technology, Xi'an, 710055, China

b. School of Energy and Power Engineering, Key Laboratory of Ocean Energy Utilization and Energy Conservation of Ministry of Education, Dalian University of Technology, Dalian 116024, China

c. Institute of Science and Technology for New Energy, Xi'an Technological University, Xi'an, 710021, China

† These authors contributed equally

*Corresponding Author:

Xiaohu Ren, renxiaohu@xauat.edu.cn

Lin Li, lilinnd@dlut.edu.cn

Mingchang Zhang, zhangmingchang@xatu.edu.cn

Supplementary Note 1.

Exfoliation of vermiculite

In this study, a two-step ion-exchange stripping strategy was successfully employed for the controlled preparation of VM nanosheets. Structural characterization revealed **(Figure S1a)** that the pristine thermally expanded vermiculite particles showed a typical lamellar stacking structure, and a stable colloidal dispersion system of vermiculite nanosheets was obtained by the synergistic action of the two-step ion intercalation method0 and ultrasound **(FigureS1b)**, whose significant Tyndall effect confirmed the formation of nanoscale particles. XRD mapping analysis **(Figure S1c)** revealed the key structural evolution: three characteristic diffraction peaks existed for the pristine vermiculite at 2θ = 6.2°, 7.4 ° and 8.9°, where three characteristic diffraction peaks are present, corresponding to the periodically aligned structure of the interlayer hydrated cations (Mg^{2+}). After ion-exchange stripping, only the characteristic peak of (001) crystal surface was retained, indicating that the interlayer cations were effectively removed and accompanied by interlayer swelling effect. Atomic force microscopy (AFM) characterization **(Figure S1d)** confirms that the exfoliated products are large-sized 2D nanosheets with lateral dimensions up to 2 μm and an average thickness of 3.8 nm, and Fig. f shows that the vermiculite nanosheets have a surface zeta potential up to -42.3 mV. This strong negativity arises from the permanent structural negative charge generated by the homocrystalline substitution of Al^{3+} for Si^{4+} in the laminate octahedra.

Preparation of bottom electrode.

Firstly, the conductive carbon nanotubes (CNTs) paste was uniformly coated on the surface of PET substrate by brush scraping method, and dried and cured at room temperature. Then, the acid-modified carbon nanotube dispersion was applied three times on the surface of the substrate, and the solvent volatilization process was performed at each drop coating interval of 15 minutes. Through this gradient functionalization strategy, the composite electrode interface with hierarchical structure is finally obtained.

Supplementary Note 2.

Equations and parameters for finite-element method calculations:

To investigate the electrodynamics of the SVA-MEG power generation process, a 3D geometric model for wet air-driven SVA-MEG power generation was developed by coupling the Nernst-Planck equation with the Poisson equation, and finite element simulations were performed. For the Nernst-Planck equation, J_i is the flux vector of the ion concentration determined by the convective flux, concentration diffusion, and electromigration flux

$$J_i = n_i u - D_i \nabla n_i - \frac{z_i e n_i D_i}{k_b T} \nabla \varphi \tag{1}$$

where n_i is the proton concentration, u is the fluid velocity, D_i is the diffusion coefficient, z_i is the valence, e is the elementary charge, k_b is the Boltzmann constant, T is the temperature, and φ is the double electric layer potential. Based on the Gauss electrostatic theorem, the Poisson equation is given

$$\nabla(\varepsilon_r \varepsilon_0 \nabla \varphi) = -\rho_e u = -F \sum_{i=1}^{N} z_i n_i \tag{2}$$

where ε_r is the dielectric constant of the water, ε_0 is the permittivity of vacuum, ρ_e is the density of electrostatic charge, and F is the Faraday constant.

The two Equations can be numerically solved with the aid of COMSOL software so as to determine the proton concentration and potential distribution. In the numerical simulation, the permittivity of PSS/PVA is assumed to be 60 and of the SA/VM aerogel is assumed to be 6. To facilitate simulations, SVA-MEG is idealized as a cylinder with a radius of 10mm and a diameter of 4.4 mm, where the PSS/PVA has a thickness of 0.1mm. It is assumed that our system can be quantitatively explained by the equations with appropriate boundary conditions. The simulated temperature is 298 K, the diffusion coefficient of water is $1e^{-12}$ m^2/s at PSS/PVA. The diffusion coefficient of proton is 0.5 e^{-13} m^2/s at SA/VM aerogel. The proton flux and potential at boundaries satisfies the condition.

$$\vec{n} \cdot J_i = 0 \quad \text{and} \quad \vec{n} \cdot \vec{D} = 0 \tag{3}$$

To describe the dissociation of protons from the SVA-MEG after water infiltrating, a chemical reaction, $RSO_3H + H_2O \Leftrightarrow RSO_3^- + H_3O^+$, is employed in the SVA-MEG domain by the "chemistry" module. The reaction rate constant is described using the Arrhenius equation. The concentration of surface functional groups (RSO_3H) in the SVA-MEG domain was set to is 1×10^{-8} mol/m^{-3}.

Supplementary Note 3

The energy conversion properties of the SA/VM aerogel are studied by measuring *I*−*V* curves in presence of a transmembrane salinity gradient. The Figure S19a shows the equivalent circuit of the membrane. V_{OC}, V_{redox}, E_{diff}, and the $R_{SA/VM\ aerogel}$ represent the measured open-circuit voltage, the redox potential generated by the unequal potential drop at the electrode-solution interface, the diffusion potential contributed by the cation selective VM-CNF/CNT membrane, and the internal resistance of the membrane, respectively. The measured V_{OC} actually consists of two parts: V_{redox} and E_{diff}, which satisfy the following equation:

$$V_{OC} = V_{redox} + E_{diff} \tag{4}$$

In this work, the generated osmotic voltage and osmotic current were obtained by subtracting the contribution from the redox potential on Ag/AgCl electrodes in different concentrations.

The transference number tn is calculated following the equation.

$$t_+ = \frac{1}{2}\left(\frac{E_{diff}}{\frac{RT}{zF}\ln\left(\frac{\gamma_{CH}c_H}{\gamma_{CL}c_L}\right)} + 1\right) \tag{5}$$

where t_+ is the cation transference number; Ediff refers to the diffusion potential; R, T, z, F, refer to the universal gas constant, absolute temperature, valence charge and Faraday constant, respectively; γ and c refer to ion activity coefficient and concentration. The KCl aqueous solution with different concentration and the ion activity coefficients of dilute solutions could be calculated using the simplified Debye-Hückel equation.

$$\lg\gamma_{\pm} = -A|z_+ z_-|\sqrt{I} \tag{6}$$

where γ± is ion average activity coefficient, 'I' is the ionic strength, z is ion valence number, and A is constant, the value is about 0.509 at 298 K.

Theoretical study

All-electron DFT calculations have been carried out by the latest version of ORCA quantum chemistry software (Version 6.1.0)[1]. The B3LYP functional[2-5] was adopted for all calculations. For geometry optimization calculation, the def2-SVP basis set[6] was used, and the optimal geometry for each compound was determined. The single point energy calculations were performed with a larger basis set the def2-TZVP basis set[7] The DFT-D3 dispersion correction with BJ-damping[8] was applied to correct the weak interaction to improve the calculation accuracy. The SMD implicit solvation model[9] was used to account for the solvation effect.

Then, the interaction energy between XX and XX were calculated by the following formula: $E_{bind}=E_{complex}-(E_{partA}+E_{partB})$

ESP analysis was performed by Multiwfn package[10].

The visualization of the ESP analysis was achieved using VESTA software.

The migration energy barriers

To evaluate the migration energy barriers in both bulk and surface models, first-principles calculations were carried out using the CASTEP module based on density functional theory. The exchange–correlation interaction was treated within the generalized gradient approximation (GGA) using the Perdew–Burke–Ernzerhof (PBE) functional. The ion–electron interactions were described using ultrasoft pseudopotentials. A plane-wave cutoff energy of 400 eV was applied after conducting convergence tests. Geometry optimization was performed until the total energy and atomic forces were less than 1×10^{-5} eV/atom and 0.03 eV/Å, respectively. For the slab models, a sufficiently large vacuum thickness (>15 Å) was introduced to avoid artificial interactions between periodic images. The minimum energy migration pathway and corresponding activation energy barriers were calculated using the Linear Synchronous Transit/Quadratic Synchronous Transit (LST/QST) method as implemented in CASTEP, where the transition states were further refined through iterative energy

minimization. All Brillouin zone integrations were performed using Monkhorst–Pack k-point meshes chosen according to the structural dimensions to ensure reliable total energies.

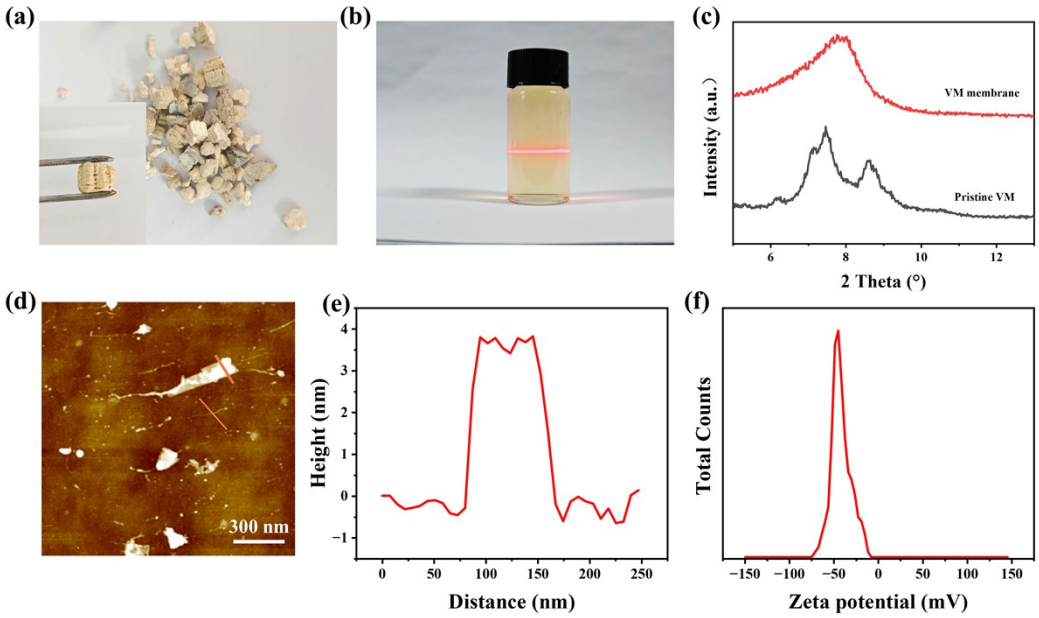

Figure S1 Preparation and characterization of vermiculite nanosheets (a) Digital photo of vermiculite particles. (b) VM nanosheet dispersion. (c) XRD images of vermiculite particles and vermiculite nanosheet films. (d) AFM images of VM nanosheets and (e) corresponding thickness curves. (f) zeta potential image of vermiculite nanosheet suspension.

Figure S2 The optical photograph of SVA-MEG.

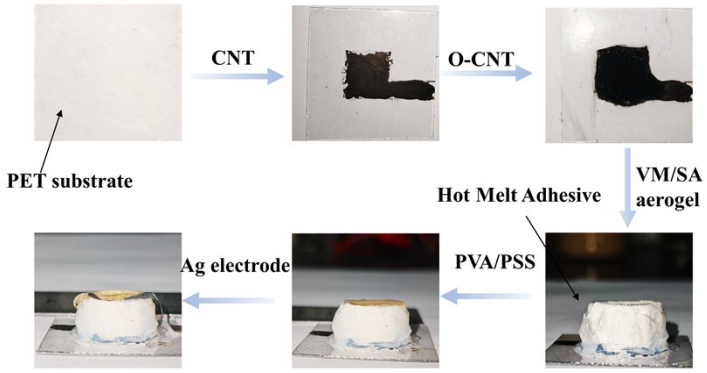

Figure S3 Schematic diagram of SVA-MEG preparation process.

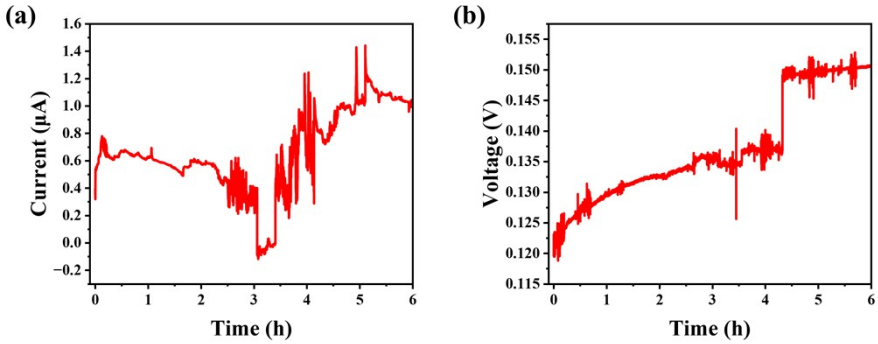

Figure S4. The electrical output performance of SVA-MEG devices without the implementation of any sealing strategy

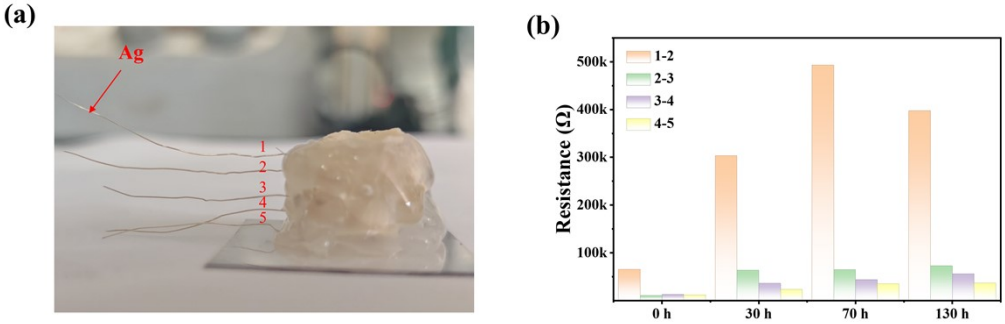

Figure S5 (a) Schematic illustration of the test setup, with the SVA-MEG sealed around its perimeter using hot melt adhesive. (b) Resistance measured between two electrodes at time points of 0 h, 30 h, 70 h, and 130 h.

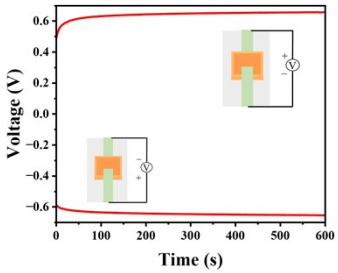

Figure S6 Effect of electrode inversion on V_{OC} output.

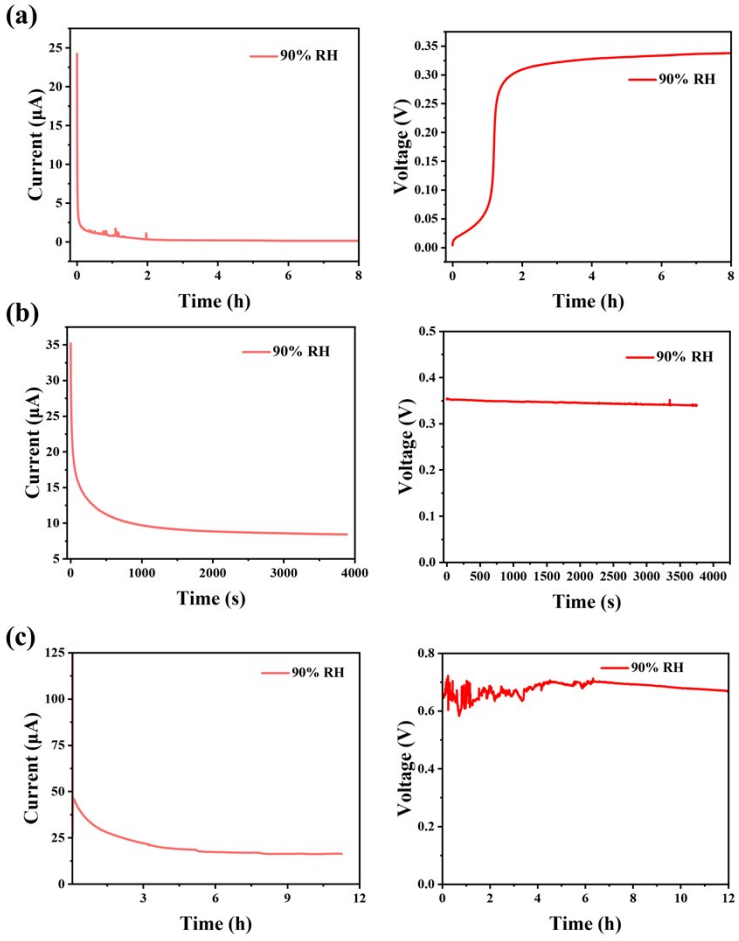

Figure S7 V_{OC} and I_{SC} curve of PSS/PVA (a) SA/VM aerogel (b) and SVA-MEG (c) with time at 90% RH.

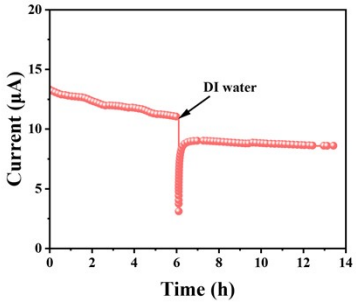

Figure S8 The curve of I_{SC} change when adding deionized water.

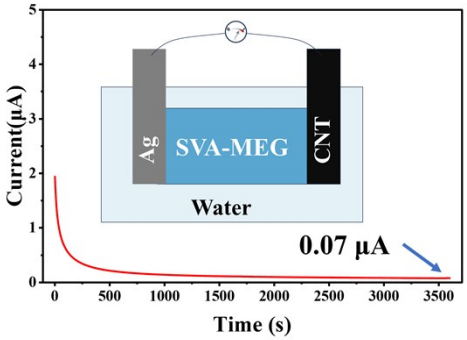

Figure S9 The I_{SC} current versus time for the SVA-MEG device immersed in DI water.

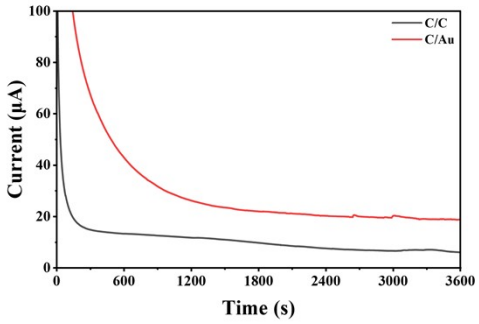

Figure S10 The I_{SC} output curves of SVA-MEG with C-C/Au-C electrodes

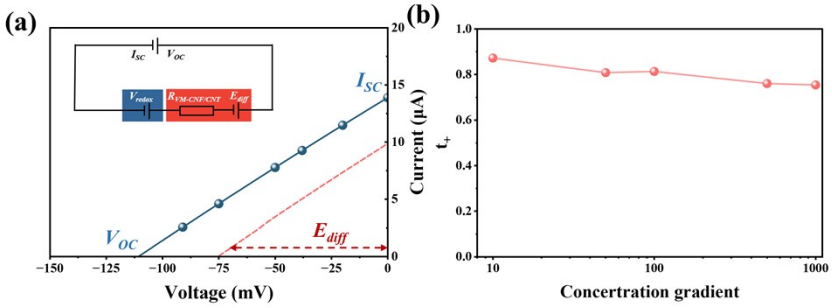

Figure S11 Comparison of the effect of the position and number of hygroscopic layers on the I_{SC}. (a) Schematic diagram of the hygroscopic layer at the top and(b) bottom with corresponding current change I_{SC}.

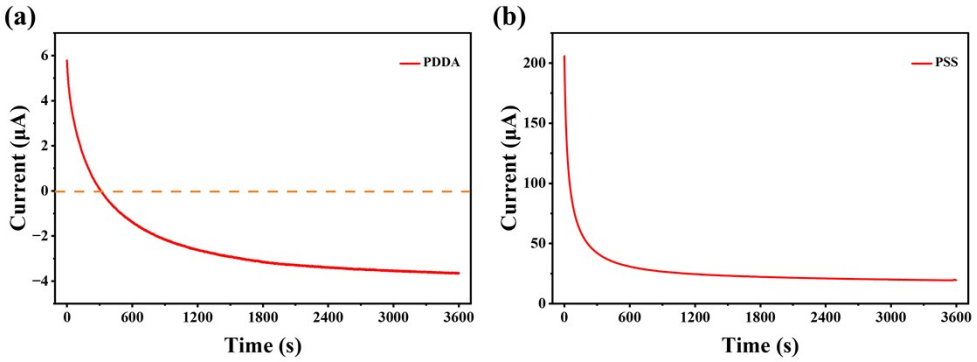

Figure 12. Output current curves of the device when the top moisture-absorbing layer is PDDA and PSS respectively.

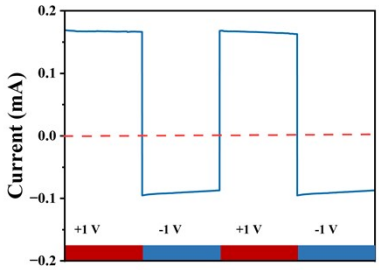

Figure S13. *I-T* curves of SVA-MEG at 80% RH with an external bias alternating
between +1 and −1V.

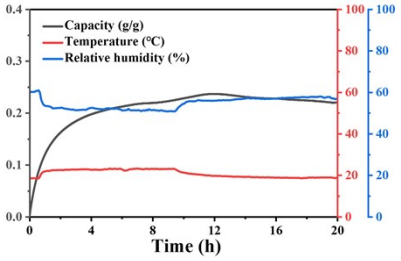

Figure S14 Hygroscopic dynamics of SVA-MEG.

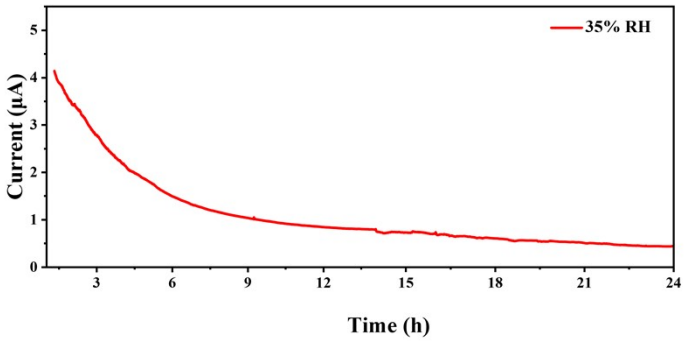

FigureS15 The I_{SC} output curve of the SVA-MEG device measured at 35%RH.

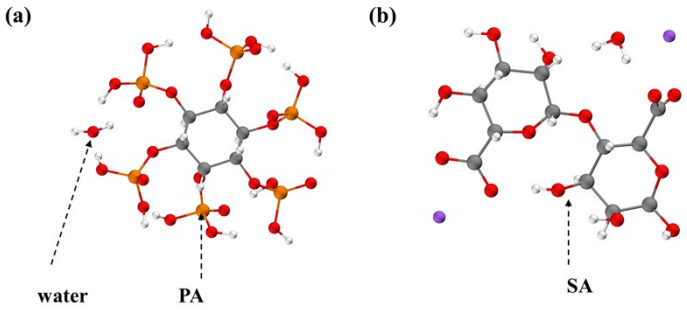

Figure S16 The corresponding interaction schematic (a) PA-H_2O and (b)SA-H_2O.

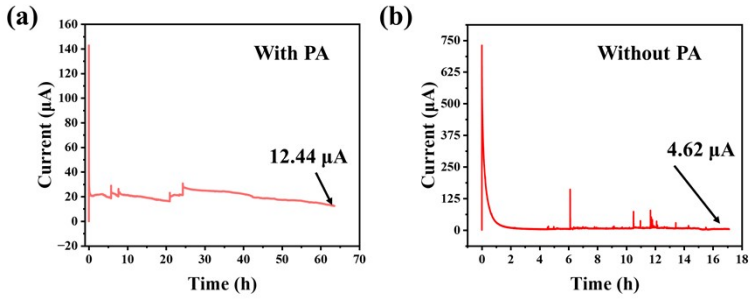

Figure S17 V_{OC} and I_{SC} of SVA-MEG w/o PA were measured at 90% RH.

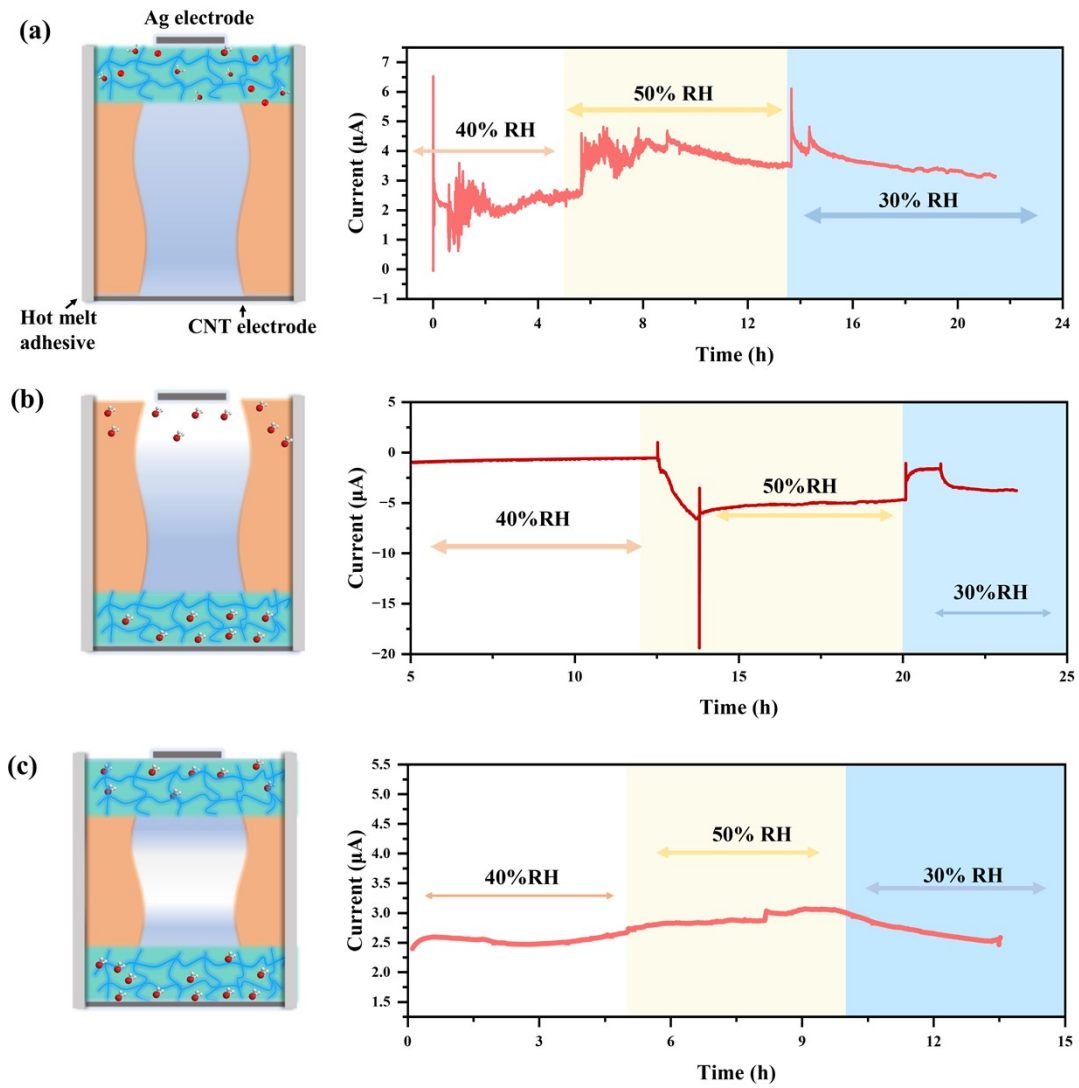

Figure S18 Comparison of the effect of the position and number of hygroscopic layers on the I_{SC}. (a) Schematic diagram of the hygroscopic layer at the top and(b) bottom with corresponding current change I_{SC}. (c) Schematic diagram of the hygroscopic layer at the top and bottom with corresponding I_{SC} curve.

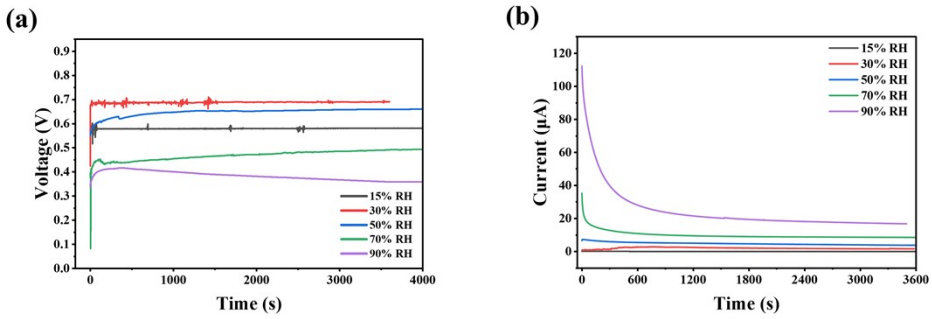

Figure S19 The curves of the V_{OC} (a) and I_{SC} (b) of SVA-MEG with time under RH conditions of 15%, 30%, 50%, 70%, and 90%.

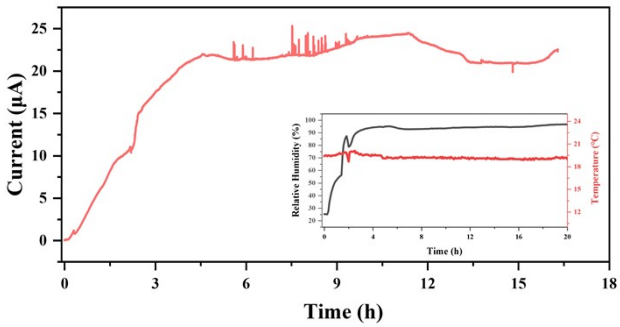

Figure S20 The I_{SC} curve at 90% RH after short-circuit connection and vacuum treatment.

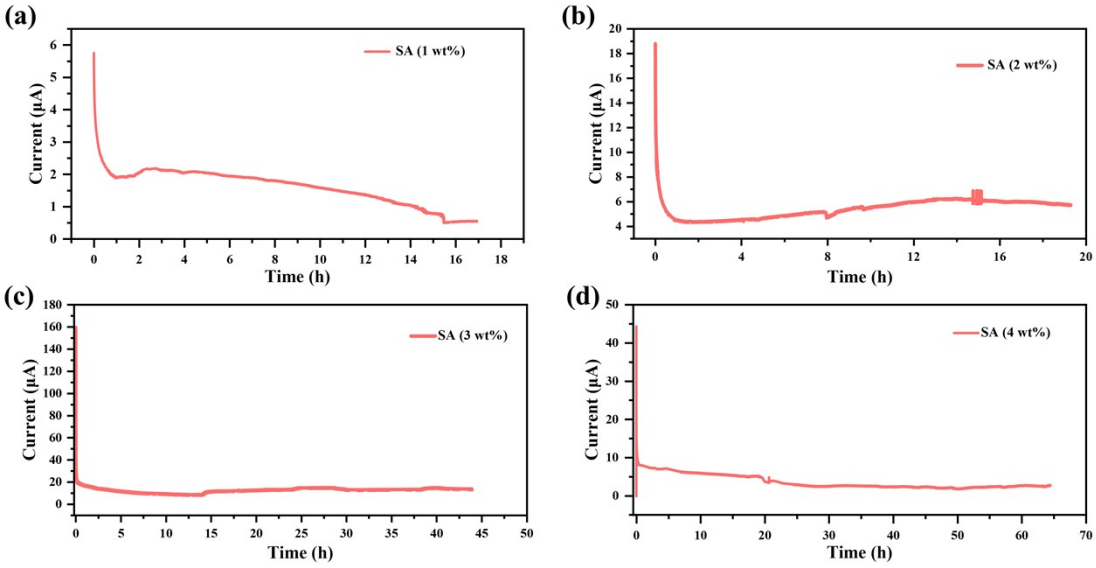

Figure S21 The I_{SC} curve of SVA-MEG with different contents of SA at 90% RH.

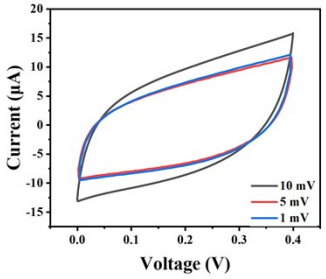

Figure S22 The Cyclic Voltammetry of SVA-MEG at different sweep speeds.

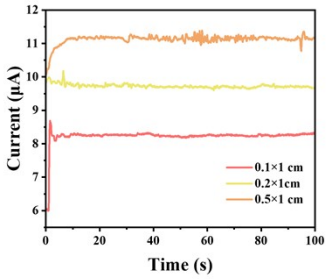

Figure S23 Effect of different size of top electrode on I_{SC}.

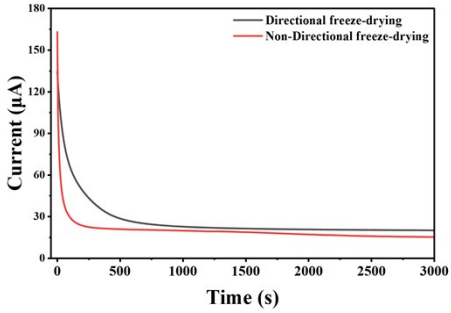

Figure S24 The I_{SC} output of directional and non-directional freeze-dried aerogels is compared.

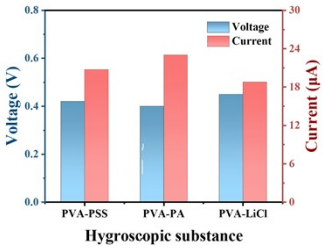

Figure S25 Comparison of the electrical output performance of SVA-MEG with PSS/PVA, PVA-PA, and PVA-LiCl Hygroscopic Layers.

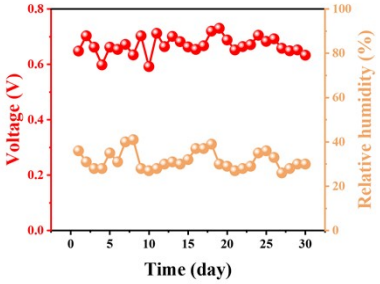

Figure S26 The V_{OC} of SVA-MEG was tested continuously for one month.

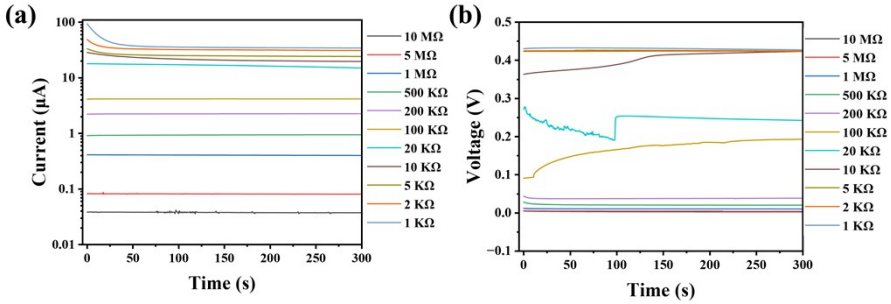

Figure S27 Curve of voltage and current with time under different resistance at 90% RH. (a) Current curve. (b) Voltage curve.

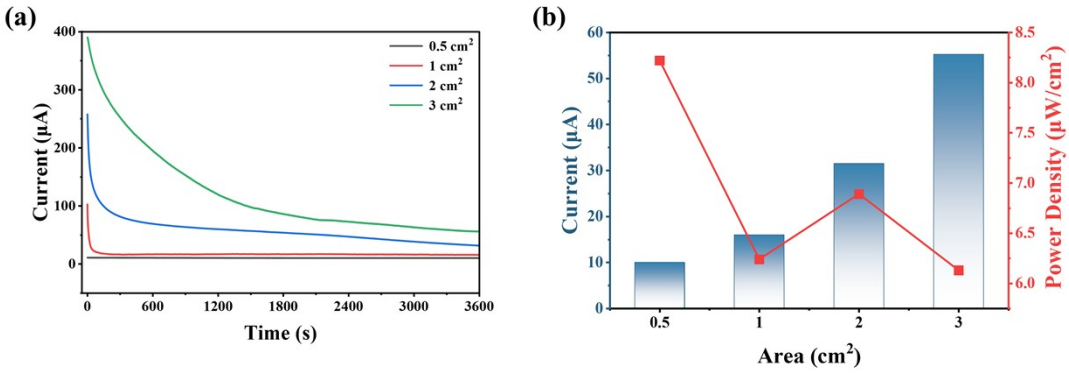

Figure S28 (a) The I_{SC} output curves for SVA-MEG devices of different areas. (b) The I_{SC} output and power density of SVA-MEG with different device areas.

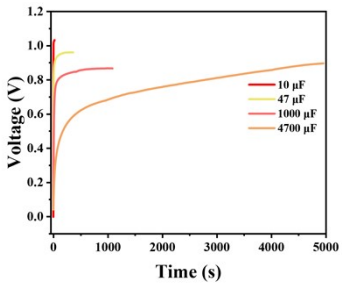

Figure S29 SVA-MEG charging curves for different capacitors.

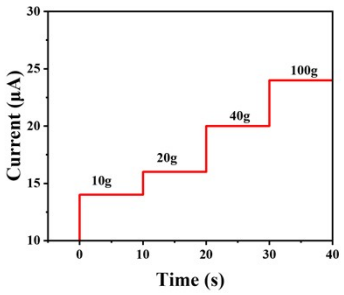

Figure S30 The I_{SC} output effect of applying different weights to the top of SVA-MEG.

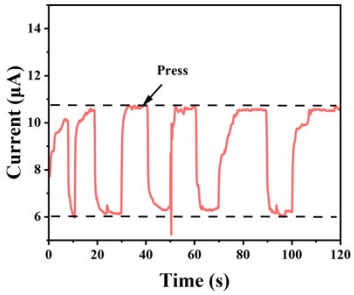

Figure S31 Curve of I_{SC} change when pressure is applied and released at the top of the device.

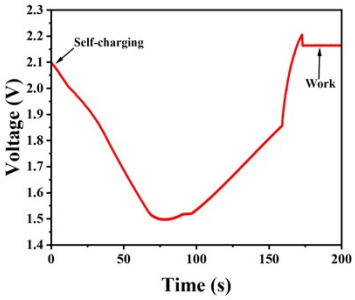

Figure S32 SVA-MEG provides intermittent power to energy management devices.

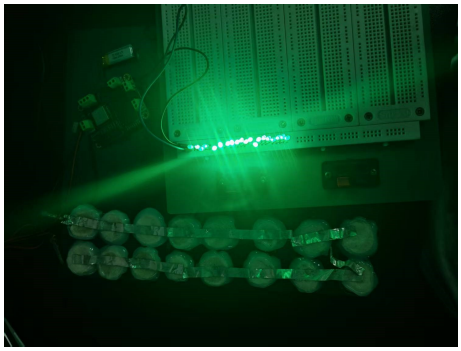

Figure S33 SVA-MEG array with 14 units powering LEDs.

Supplementary table S1

Concentration gradient (mM/mm)	1/10	1/50	1/100	1/500	1/1000
V_{OS} (mV)	44	62	74	83	90
V_{thero} (mV)	53	105	118	166	174
Transference number (t_+)	0.872	0.808	0.813	0.760	0.754

Supplementary table S2

V_{OC}	I_{SC}	**Continuous work time**	**Relative Humidity (%)**	**Ref**	**Electrode**
1 V	1.79 μA/cm^2	4.17 h	90%	[11]	C
1.1 V	17 nA/cm^2	11.7 h	30%	[12]	C
0.4 V	1.5 μA/cm^2	8.3 h	80%	[13]	Au
1.2 V	50 nA/cm^2	258 h	30%	[14]	C
0.5 V	0.25 μA/cm^2	140 h	80%	[15]	Reassembled Graphite
0.4 V	0.12 μA/cm^2	8 h	90%	[16]	ITO
1.1 V	2.6 μA/cm^2	13.9 h	90%	[17]	C/Al
0.4 V	1.75 μA/cm^2	3.3 h	95%	[18]	Ag
1.25 V	2.52μA/cm^2	100 h	90%	[19]	Zn/C
0.34 V	1 μA/cm^2	9 h	80%	[20]	C
0.26 V	2.59μA/cm^2	168 h	70%	[21]	C
0.72 V	10.44 μA/cm^2	＞240 h	90%	This work	Ag/C

References:

[1] Neese, F. Software Update: The ORCA Program System—Version 6.0. *WIR Es Computational Molecular Science* **2025**, *15* (2), e70019. DOI: https://doi.org/10.1002/wcms.70019.

[2] Becke, A. D. Density-functional thermochemistry. III. The role of exact exc hange. *The Journal of Chemical Physics* **1993**, *98* (7), 5648-5652. DOI: https://doi.org/10.1063/1.464913.

[3] Lee, C.; Yang, W.; Parr, R. G. Development of the Colle-Salvetti correlati on-energy formula into a functional of the electron density. *Physical Revie w B* **1988**, *37* (2), 785-789. DOI: https://doi.org/10.1103/PhysRevB.37.785.

[4] Vosko, S. H.; Wilk, L.; Nusair, M. Accurate spin-dependent electron liquid correlation energies for local spin density calculations: a critical analysis. *Canadian Journal of Physics* **1980**, *58* (8), 1200-1211. DOI: https://doi.org/10.1139/p80-159.

[5] Stephens, P. J.; Devlin, F. J.; Chabalowski, C. F.; Frisch, M. J. Ab Initio Calculation of Vibrational Absorption and Circular Dichroism Spectra Usin g Density Functional Force Fields. *The Journal of Physical Chemistry* **199 4**, *98* (45), 11623-11627. DOI: https://doi.org/10.1021/j100096a001.

[6] Weigend, F.; Ahlrichs, R. Balanced Basis Sets of Split Valence, Triple Zeta Valence and Quadruple Zeta Valence Quality for H to Rn: Design and ass essment of accuracy. *Physical Chemistry Chemical Physics* **2005**, *7* (18), 3 297-3305, 10.1039/B508541A. DOI: https://doi.org/10.1039/B508541A.

[7] Binkley, J. S.; Pople, J. A.; Hehre, W. J. Self-consistent Molecular Orbital Methods. 21. Small split-valence basis sets for first-row elements. *Journal of the American Chemical Society* **1980**, *102* (3), 939-947. DOI: https://doi.org/10.1021/ja00523a008.

[8] Grimme, S.; Ehrlich, S.; Goerigk, L. Effect of the Damping Function in Di spersion Corrected Density Functional Theory. *J Comput Chem* **2011**, *32* (7), 1456-1465. DOI: https://doi.org/10.1002/jcc.21759.

[9] Marenich, A. V.; Cramer, C. J.; Truhlar, D. G. Universal Solvation Model Based on Solute Electron Density and on a Continuum Model of the Solvent

Defined by the Bulk Dielectric Constant and Atomic Surface Tensions. *The Journal of Physical Chemistry B* **2009**, *113* (18), 6378-6396. DOI: https://doi.org/10.1021/jp810292n.

[10] Lu, T.; Chen, F. Multiwfn: a Multifunctional Wavefunction Analyzer. *J C omput Chem* **2012**, *33* (5), 580-592. DOI: https://doi.org/10.1002/jcc.22885 .

[11] He, W.; Wang, H.; Huang, Y.; He, T.; Chi, F.; Cheng, H.; Liu, D.; Dai, L.; Qu, L. Textile-based Moisture Power Generator with Dual Asymmetric Structure and High Flexibility for Wearable Applications. *Nano Energy* **20 22**, *95*, 107017. DOI: https://doi.org/10.1016/j.nanoen.2022.107017.

[12] Zhao, K.; Li, S.; Zan, G.; Kim, G.; Jiang, W.; Park, J. W.; Yoon, J.; Oh, J. H.; Jang, J.; Lee, S.; et al. Moisture-driven Energy Generation by Verti cally Structured Polymer Aerogel on Water-collecting gel. *Nano Energy* **20 24**, *126*, 109645. DOI: https://doi.org/10.1016/j.nanoen.2024.109645.

[13] Long, Y.; He, P.; Shao, Z.; Li, Z.; Kim, H.; Yao, A. M.; Peng, Y.; Xu, R.; Ahn, C. H.; Lee, S.-W.; et al. Moisture-induced Autonomous Surface Potential Oscillations for Energy Harvesting. *Nature Communications* **2021**, *12* (1), 5287. DOI: https://doi.org/10.1038/s41467-021-25554-y.

[14] Wang, H.; Sun, Y.; He, T.; Huang, Y.; Cheng, H.; Li, C.; Xie, D.; Yang, P.; Zhang, Y.; Qu, L. Bilayer of Polyelectrolyte Films for Spontaneous Po wer Generation in air up to an Integrated 1,000 V output. *Nature Nanotec hnology* **2021**, *16* (7), 811-819. DOI: https://doi.org/10.1038/s41565-021-00903-6.

[15] Moreira, K. S.; Lermen, D.; dos Santos, L. P.; Galembeck, F.; Burgo, T. A. L. Flexible, Low-cost and Scalable, Nanostructured Conductive Paper-ba sed, Efficient Hygroelectric Generator. *Energy & Environmental Science* **20 21**, *14* (1), 353-358, 10.1039/D0EE03111A. DOI: https://doi.org/10.1039/D0EE03111A.

[16] Yang, Y. n.; Wang, J.; Wang, Z.; Shao, C.; Han, Y.; Wang, Y.; Liu, X.; Sun, X.; Wang, L.; Li, Y.; et al. Moisture-Electric–Moisture-Sensitive Hete rostructure Triggered Proton Hopping for Quality-Enhancing Moist-Electric Generator. *Nano-Micro Letters* **2023**, *16* (1), 56. DOI: https://doi.org/10.1007/

s40820-023-01260-w.

[17] He, T.; Wang, H.; Lu, B.; Guang, T.; Yang, C.; Huang, Y.; Cheng, H.; Qu, L. Fully Printed Planar Moisture-enabled Electric Generator Arrays for sCalable Function Integration. *Joule* **2023**, *7* (5), 935-951. DOI: https://doi.org/10.1016/j.joule.2023.04.007.

[18] He, W.; Li, P.; Wang, H.; Hu, Y.; Lu, B.; Weng, C.; Cheng, H.; Qu, L. Robustly and Intrinsically Stretchable Ionic Gel-Based Moisture-Enabled Po wer Generator with High Human Body Conformality. *ACS Nano* **2024**, *18* (19), 12096-12104. DOI: https://doi.org/10.1021/acsnano.3c08543.

[19] Zhou, J.; Ren, Z.; Cui, X.; Liu, X.; Lu, X. Bioinspired Interfacial Design of Robust Aramid Nanofiber Composite Films for High-Performance Moist ure-Electric Generators. *Advanced Energy Materials* **2025**, *15* (25), 240484 0. DOI: https://doi.org/10.1002/aenm.202404840 (acccessed 2025/12/01).

[20] Xu, C.; Fu, C.; Jiang, Z.; Yang, T.; Xin, M. Hygroelectric Generator Bas ed on Antisymmetric Modification of Graphene Spheres with Ionic Hydrog els. *ACS Applied Nano Materials* **2023**, *6* (7), 5930-5938. DOI: https://doi.org/10.1021/acsanm.3c00314.

[21] Fang, J.; Zhao, Z.; Xu, Z.; Ni, Q. Large-scale and Continuous Production of Sodium Alginate/MWCNTs Axial Heterogeneous Fibers Moisture-electric Generator with Visual Identification of Acid/alkali Gases. *International Jou rnal of Biological Macromolecules* **2025**, *322*, 146897. DOI: https://doi.org/10.1016/j.ijbiomac.2025.146897.